Research Square

Preprints are preliminary reports that have not undergone peer review.
They should not be considered conclusive, used to inform clinical practice,
or referenced by the media as validated information.

Electrically Tunable Selectivity Enhancement Overcomes the Permeability-Selectivity Trade-off in Two-dimensional Nanofluidic Channels

Wanqi Zhou
Nanjing University of Aeronautics and Astronautics
Wanlin Guo
Nanjing University of Aeronautics and Astronautics
Hu Qiu
qiuhu@nuaa.edu.cn
Nanjing University of Aeronautics and Astronautics

Research Article

Keywords: Reverse osmosis, Nanoslit channel, Ion selectivity, MD Simulations

Posted Date: August 26th, 2026

DOI: https://doi.org/10.21203/rs.3.rs-10811960/v1

License: This work is licensed under a Creative Commons Attribution 4.0 International License.
Read Full License

Additional Declarations: The authors declare no competing interests.

Electrically Tunable Selectivity Enhancement Overcomes the Permeability-Selectivity Trade-off in Two-dimensional Nanofluidic Channels

Wanqi Zhou[1], Wanlin Guo[1] and Hu Qiu[1,*]

ABSTRACT

Membrane-based desalination and other separation processes are suffering from a ubiquitous, pernicious trade-off between selectivity and permeability, *i.e.*, high selectivity comes at the expense of reduced permeability, and vice versa. Here we show that applying an external electric field can drastically enhance the salt rejection rate of two-dimensional nanofluidic channels from approximately 84%—a level unsuitable for commercial use—to as high as 99.5%, while leaving the water flow rate unaffected, thereby overcoming the permeability-selectivity trade-off. Through extensive molecular dynamics simulations and free energy calculations, we reveal that the enhanced selectivity arises from the field-induced reorientation of the hydration shells surrounding confined ions within the nanochannels, which significantly modulates the electrostatic interactions between the ions and their own hydration layers, thereby increasing the associated energy barriers. We further show that this previously unidentified mechanism is universally applicable to all major seawater ions, including Na^+, Cl^-, K^+, Ca^{2+}, Mg^{2+}, I^- and Br^-, as well as to nanofluidic channels made from graphene, hexagonal boron nitride and graphene oxide. This work offers a powerful strategy to tune membrane selectivity without compromising permeability, offering substantial potential to transform membrane-based separation technologies.

Keywords: Reverse osmosis, Nanoslit channel, Ion selectivity, MD Simulations

Introduction

Fresh water has been an increasingly scarce resource due to population growth, industrialization and climate change. Due to the vast amount of seawater on Earth, desalinating the saline water of seas and oceans to produce fresh water has become an important strategy to meet the demand for clean water supply [1]. Currently, membrane-based technologies such as reverse osmosis (RO), where water is pushed through a semi-permeable membrane under pressures, while salts and other solutes are retained, have been widely used throughout the world for desalination and water treatment [2,3]. State-of-the-art polymeric RO membranes such as thin-film composite (TFC) membrane fulfill the salt rejection process based on the difference in rates of species (*i.e.*, water and ions) to dissolve into and diffuse through the membrane material, known as the solution-diffusion mechanism [1]. However, these membranes typically exhibit an inherent trade-off between permeability and selectivity, *i.e.*, a more permeable RO membrane material usually exhibits a lower salt rejection rate, and vice versa. Moreover, these conventional membranes suffer from practical challenges such as fouling [1], degradation [1,4], and limited selectivity [5,6]. To overcome these limitations, there has been significant interest in the search for alternative membrane materials.

The observation of fast permeation of water through various nanoporous materials, such as porous graphene/MoS_2 [7–16], graphyne [17, 18], carbon nanotubes (CNTs) [19–27], nanoslit channels [28–31], and graphene oxide (GO) membranes [32–35] has led to many proposals to use these materials as novel RO membranes. The rigid, well-defined nanopores in these membranes allow smaller water molecules to pass through, while larger particles are impeded due to size exclusion. However, these membranes typically have a nonuniform pore size distri-

[1]Key Laboratory for Intelligent Nano Materials and Devices of Ministry of Education, State Key Laboratory of Mechanics and Control for Aerospace Structures, Nanjing University of Aeronautics and Astronautics, Nanjing 210016, China

[*]**Corresponding authors.**
Email: qiuhu@nuaa.edu.cn.

Received: XX XX Year;
Revised: XX XX Year;
Accepted: XX XX Year

© The Author(s) Year. Published by Oxford University Press on behalf of China Science Publishing & Media Ltd. This is an Open Access article distributed under the terms of the Creative Commons Attribution License (http://creativecommons.org/licenses/by/4.0/), which permits unrestricted reuse, distribution, and reproduction in any medium, provided the original work is properly cited.

bution, leading to limited salt rejection when used for desalination [35,36]. There have been a number of attempts to promote selectivity of nanoporous membranes through precisely controlling pore size. For example, the interlayer spacing of GO membranes can be modulated by introducing or strengthening covalent bond, π–π interaction, or electrostatic interaction between the GO nanosheets [37,38]; uniform nanopores can be formed within grain boundaries on MoS_2 by precisely controlling MoS_2 grains during the synthesis through chemical vapor deposition [39]. Despite much progress, the formation of a high density of uniform nanopores over large areas remains a major challenge for these nanoporous membranes, limiting their separation performance. Therefore, bypassing the need for precise pore size control and developing an easily implementable and universal strategy to overcome the permeability-selectivity issue presents a promising route for significantly promoting the membrane performance. For this purpose, various strategies involving the application of external fields have been proposed to regulate ion selectivity of nanoporous membranes. Specifically, applying an external electric field can drive ions either upstream against the water flow or laterally toward the channel sidewalls, thereby enabling effective ion separation and improved selectivity [40–43]. Other approaches include exploiting surface slip at the liquid–graphene interface to enhance selectivity [44,45], applying an electromagnetic field to induce ion precipitation [46], and introducing net charged sites within nanochannels to selectively repel specific ions [47]. However, these approaches usually require complex channel designs or are effective only for specific types of ions.

In this work, we show that an external field can polarize the hydration shells of confined ions in two-dimensional nanoslit channels, significantly enhancing the salt rejection, without compromising water permeability. This novel mechanism, applicable to all major seawater ions including Na^+, Cl^-, K^+, Ca^{2+}, Mg^{2+}, I^- and Br^-, as well as to nanofluidic channels made of graphene, hexagonal boron nitride (*h*-BN) and GO, offers a simple, yet universal way to overcome the permeability-selectivity trade-off, eliminating the need for complex channel designs. Moreover, the ion selectivity can be tuned by adjusting the field strength, enabling active and programmable control over concentration—a highly desirable feature for advanced electrochemical systems.

Results

Enhanced salt rejection of nanoslit channels under an electric field

In RO processes, the feed solution should be pressurized and driven across a semipermeable membrane containing an array of nanoslit channels, producing a purified permeate on the opposite side, as shown in the top panel of Fig. 1a. Owing to computational limitations that restrict the accessible length and time scales in atomistic simulations, we chose to simulate the RO process based on an individual channel, as shown in the bottom panel of Fig. 1a. Specifically, the system contains a graphene nanoslit channel formed by two parallel graphene sheets in contact with two reservoirs filled with 1 M NaCl solution at both ends of the channel (see details in Methods section). We primarily focused on a channel of 9.2 Å in height, and also considered wider channels to verify the robustness of our findings. A relatively high external pressure of 100 MPa was applied in MD simulations to ensure convergence of data in limited time scale, and additional simulations at 10 and 50 MPa shows qualitatively consistent results (Fig. S1). An electric field along the x direction was applied in the membrane region. The field strength, E, was ranged from 0.05 to 1.0 V/nm, which should be experimentally accessible [48]. Other simulation details can be found in Methods section.

We first carried out a series of simulations with a system containing 1 M NaCl, and plotted the salt rejection and water permeability as functions of the field strength E in Figs. 1b and c, respectively. Herein, the salt rejection rate was determined through $[1 - (n_{p,i}/n_i)/(n_{p,w}/n_w)]\times100\%$, where $n_{p,i}$ ($n_{p,w}$) and n_i (n_w) are the number of ions (water molecules) passing through the nanoslit channel and in the bulk solution, respectively (see Methods for details). In the absence of an electric field, both Na^+ and Cl^- can permeate through the nanoslit channel, with a relatively low salt rejection rate at 84.33%. This observation aligns with the previous experiments showing that only much narrower (~3.4 Å) channels can achieve perfect ion rejection [31]. With the increase of E, the salt rejection increases substantially (Fig. 1b). In particular, under E = 1.0 V/nm, the salt rejection reaches 99.5%, comparable with those (>99%) for typical commercial RO and nanofiltration membranes [49]. The salt rejection can be further promoted to 100% (Fig. S1), if the driving pressure is reduced to 50 or 10 MPa (still higher than those adopted in commercial RO systems). At the same time,

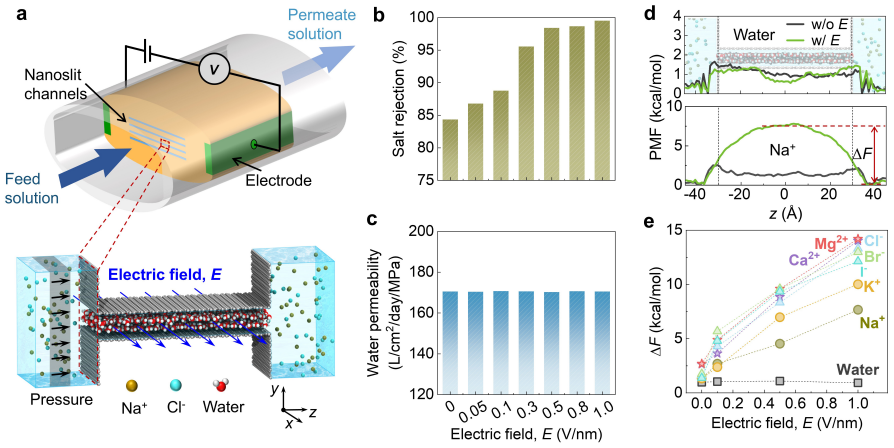


Figure 1. Enhanced salt rejection of nanoslit channels under an electric field. **(a)** Schematic illustration of the RO process based on a membrane containing nanoslit channels (top panel). The bottom panel shows the molecular dynamics (MD) simulation system of such a process whereby an individual nanoslit channel with an interlayer distance (channel height) of 9.2 Å is placed between two reservoirs filled with 1 M NaCl solution. An external force is applied to water molecules located 15–25 Å from the left side of the nanoslit channel (indicate with black arrows) to generate a pressure of 100 MPa (see Methods for details). An electric field along the x axis is applied within the channel area. **(b) (c)** Salt rejection **(b)** and water permeability **(c)** versus the strength of the electric field. **(d)** The free energy (the potential of mean force, PMF) profiles along the channel axis (z-axis) for water and Na^+ with (green) and without (black) an electric field (E = 1.0 V/nm). **(e)** Free energy barrier (ΔF) as a function of field strength for water molecules and ions. ΔF is defined as the difference between the average free energy in channel and bulk.

the high permeability of water is found to be nearly unaffected by the field in these simulations (Fig. 1c). These findings suggest that the external field can significantly promote the salt rejection of the channel, without compromising its permeability, thus to some extent breaking the trade-off between water permeability and selectivity (Fig. S2). Furthermore, our additional simulations show that the electrically tunable selectivity enhancement is robust in various systems, such as nanoslit channels with different interlayer distances (Fig. S3) or h-BN as the channel wall material (Fig. S4), GO membranes (Fig. S5), systems employing KCl solution instead of NaCl solution (Fig. S6), and simulation setups employing piston-driven pressurization (Fig. S7).

The ability of the electric field to promote salt rejection can be further explored by computing the free energy (the potential of mean force, PMF) profiles for water and ion permeation using the umbrella sampling (US) method (see Methods for details), as shown in Fig. 1d. The energy barrier (ΔF) was defined as the difference between the average free energy in the channel and that in the bulk. For water, the energy barrier remains very low (~1.00 kcal/mol), regardless of the presence of a field, consistent with the observed high water permeability and its insensitivity to the field (Fig. 1c). In contrast, under an external field of 1 V/nm, the energy barrier for Na^+ increases markedly from 2.63 to 7.03 kcal/mol. Given that the ion permeation rate follows an exponential dependence on ΔF, this sharp rise in the energy barrier aligns with the significantly enhanced salt rejection shown in Fig. 1b. To verify the robustness of our results, we also carried out additional simulations incorporating polarization effects via the polarizable SWM4-NDP water model, which yielded consistent trends in the PMF profiles (Fig. S8).

Having computed the PMF for Na^+, we extended our analysis to nearly all major ion species present in seawater through extensive simulations (Fig. S9), and collected in Fig. 1e the determined energy barriers for these ions under various E. It is found that ΔF for all ions increases with E, whereas that for water molecules fluctuates around ~1.00 kcal/mol and is independent of E. These results suggest that a sufficiently high electric field could, in principle, achieve complete rejection of these ions.

Hydration-shell reorientation enhances selectivity

We now examine the origins of ion selectivity in detail. In the absence of an electric field, the increase in free energy as the ion enters the nanoslit channel can be attributed to the dehydration process (Fig. S10), resulting in a salt rejection of 84.33%, a phenomenon that has been widely investigated [17,24,26,50]. However, the mechanism by which the electric field enhances ion selectivity (from 84.33% to 99.5%) has remained unclear. Because the applied electric

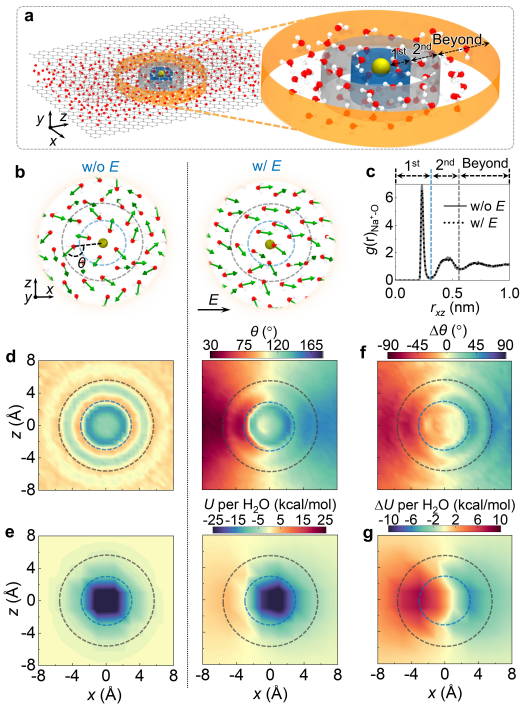


Figure 2. Field-induced reorientation of ion hydration shells. (a) Schematic illustration showing the first and second hydration shells. For clarify, the bulk solution and the vertical graphene walls are not shown. **(b)** Electric field-induced reorientation of water dipoles. The orientation angle θ is defined as the angle between the dipole of a water molecule (green arrow) and the line joining the Na^+ to water oxygen. **(c)** Lateral Na^+—oxygen radial distribution functions (RDFs) versus the lateral position r_{xz} parallel to the confining walls with (w/ E) and without (w/o E) an electric field (E = 1.0 V/nm). The first and second hydration shell comprises water molecules with r_{xz} satisfying $r_{xz} \leq 3.0$ Å (vertical blue dashed line) and $3.0 < r_{xz} \leq 5.8$ Å (vertical black dashed line), respectively. **(d)** Distribution of θ for water molecules in different positions around Na^+ [placed at (0,0)]. **(e)** Distribution of the Coulomb interaction energy (U) between Na^+ and water molecules around it. **(f)** and **(g)** Differences in θ and U caused by the action of an electric field. In panels **d-g**, the blue and black dashed lines indicate the boundaries of the first and second hydration shells, respectively. It should be noted that x and z here denote the relative positions of water molecules in the hydration shell around the central ion. All the data presented were obtained in simulations whereby the ion was deliberately constrained inside the nanochannel, allowing us to collect sufficient data for reliable statistics.

field is neither aligned with the channel axis nor perpendicular to the nanoslit walls, previously proposed mechanisms relying on these field orientations-such as ion separation driven by an electric force opposing the water flow [41], ion trapping induced by electric forces normal to the channel walls [40], and field-induced interfacial slip [44], do not apply in the present system. Meanwhile, the free-energy profiles for channels of different lengths suggest that, in the absence of an electric field, the baseline energy barrier located at the channel entrance is nearly independent of channel length (Fig. S11). In the presence of an electric field, however, the energy barrier in shorter channels is slightly lower than in longer channels, indicating that the enhanced barrier is not related to the channel entrance, but rather originates from a novel confinement–field synergy within the nanoslit channel, as will be demonstrated below.

It is known that ion selectivity in nanoconfined geometries may also be associated with the reorganization of hydration shells [51]. To examine this possibility, we analyzed the influence of the electric field on ion hydration structures (Fig. 2a to f) by conducting simulations in which an ion was deliberately constrained inside the nanochannel (in analogy to umbrella sampling simulations). We first calculated the lateral radial distribution functions (RDFs) between Na^+ ions and the oxygen atoms of water molecules inside the nanoslit channel, specifically for Na^+ ions constrained around z = 0.5 Å (Fig. 2c), and found that the resulting RDF profiles are nearly identical in the presence and absence of an applied electric field. In addition, we evaluated the coordination number of water molecules in the Na^+ hydration shells along the transport pathway (Fig. S10), and found that the hydration number remained essentially unchanged, regardless of the field strength applied. This finding allows us to rule out the dehydration effect—a common mechanism proposed in prior studies [26,50,52]—as the explanation for selectivity enhancement (from 84.33% to 99.5%) in the present work.

It has been recently shown that the field-induced reorientation of water molecules around confined ions can drastically affect the channel selectivity [48]. Taking again Na^+ as an example, we explore below how the orientation angles θ of water molecules in its hydration shells respond to the external field, with θ defined as the angle between the water dipole vector and the vector connecting Na^+ to the oxygen atom of the water molecule (Fig. 2b). The Na^+ was also deliberately constrained inside the nanochannel during the calculation, allowing us to collect sufficient data for a reliable evaluation of θ. In the absence of electric fields, water molecules in the first hydration shell preferentially orient their O atoms toward the Na^+ ion, with H atoms pointing away, as indicated by θ values exceeding 150° (left panel in Fig. 2d). This configuration results from the strong Coulomb interaction between the cation and the partial charges carried on water oxygen and hydrogen atoms. A similar, though less pronounced, orientation is ob-

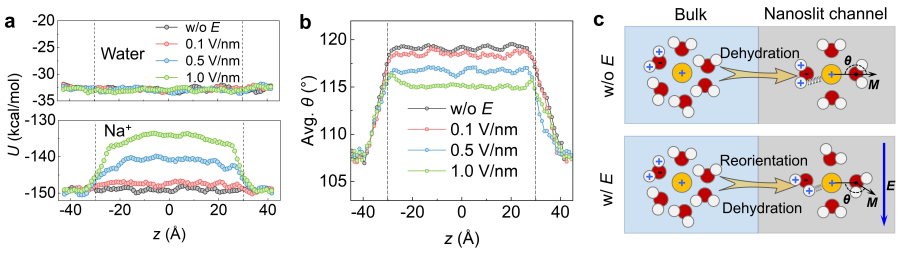


Figure 3. Enhanced Coulomb interaction energy as the origin of the increased energy barrier. (a) The top (bottom) panel shows the average Coulomb interaction energy (U) between a water molecule (Na^+ ion) and the surrounding water molecules within $r_{xz} < 12$ Å at different z-positions along the channel axis. **(b)** Average orientation angle (θ) of the water molecules within the first and second hydration shells of Na^+. The orientation angle θ is defined as the angle between the dipole of a water molecule and the line joining the Na^+ to water oxygen. **(c)** Schematic illustration of ion hydration structures in bulk solution and inside the channel, with or without an applied electric field.

served in the second hydration shell, as reflected by the relatively lower θ values. Beyond the first and second hydration shells, water molecules exhibit random orientations, resulting in an average θ around 90° (see left panels in Fig. 2b and 2d).

Upon application of an electric field, the θ distribution changes remarkably (right panels in Fig. 2b and 2d), with the extent of reorientation varying by location. Within the first hydration shell, water molecules experience subtle reorientation. This is again the signature of strong electrostatic interactions between the ion and these waters, preventing the water molecules from being reoriented. In contrast, water molecules in the second hydration shell and beyond tend to align their dipoles with the field direction. This leads to a decrease in θ for water molecules to the left of the ion ($x < 0$) and an increase for water molecules to the right ($x > 0$; see right panel in Fig. 2b). This spatial inhomogeneity in reorientation is directly evidenced by the distribution of the change in θ ($\Delta\theta$) plotted in Fig. 2f.

It is well established that the water reorientation in ions' hydration shells may alter the interaction between water and ions, thereby influencing the free energy barrier for ion permeation [53]. Here, we primarily focus on the changes in the Coulomb interaction energy (U), because it is shown to be much stronger than the van der Waals (vdW) interaction energy (Fig. S12). As shown in Fig. 2e, very strong attractive (negative) interactions exist between Na^+ and water molecules within the first hydration shell, which are insensitive to the action of the external field. The interaction becomes much weaker for water in the second hydration shell and beyond, which, however, can readily be altered by the field. For instance, under the action of the field, a repulsive (positive) interaction emerges between the ion and water to its left (red region in right panel of Fig. 2e), a feature absent in the field-free case (left panel). These spatially varying changes in the interaction energy align well with the reorientation behavior of water molecules depicted in (Fig. 2d). In addition, a direct comparison of the field-induced changes in θ and U (denoted as $\Delta\theta$ and ΔU shown in Figs. 2f and 2g, respectively) reveals a strong correlation between θ and U: U tends to increase in regions where θ increases, and decrease where θ falls.

We then placed the Na^+ ion at different z position along the channel axis and computed the average Coulomb energy U and θ between this ion and surrounding water molecules (see Methods for details), as shown in the bottom panel of Fig. 3a and Fig. 3b. Unexpectedly, the reorientation of water molecules within the ionic hydration shell is fully consistent with the enhanced Coulomb interactions between the ion and the surrounding hydration-shell water molecules along the transport pathway. As the electric field increases, the average θ inside the channel gradually decrease, whereas the Coulomb interactions progressively increase. More interestingly, the profiles of the interaction energy look incredibly similar to the PMF profiles (see Fig. 1d and Fig. S9); both profiles increase with the applied field strength. Nevertheless, the increase in the free-energy barrier appears smaller than that in the interaction energy, which can be attributed to ensemble averaging applied during the free-energy calculation, as well as to contributions from entropy and solvent reorganization [54].

The correlation between the PMF, θ, and the Coulomb interaction profiles reveals a clear molecular-level mechanism of the found ion rejection, as sketched in Fig. 3c. In the absence of an electric field, the dehydration process at the channel entrance establishes a baseline energy barrier (2.63 kcal/mol), corresponding to the ob-

served 84.33% salt rejection. Under an applied electric field, the field-induced reorientation of the ion's hydration shell enhances the Coulomb interactions between the ion and the surrounding water molecules, imposing an additional energy cost of 7.03 kcal/mol, raising the salt rejection from 84.33% to 99.5%. In contrast, the average Coulomb interaction between water molecules inside the channel remains nearly unaffected by the electric field (top panel of Fig. 3a), indicating that the free energy barrier for water entering the nanoslit channel from the bulk solution remains unchanged. Additionally, the applied electric field is insufficient to alter the overall water density or the number of hydrogen bonds (reflecting the viscosity), as shown in Fig. S13. Consequently, it does not affect the water permeability.

Discussion

To rule out the possibility that the observed mechanism arises as an artifact of the applied electric field, we carried out the following verification analyses. The trend of the strengthened Na^+-water interaction and the nearly unchanged water-water interaction under an electric field is also confirmed by our DFT calculations (Fig. S14). In the main simulations presented in this work, the external electric field was applied along the x-direction. We also carried test simulations with the field direction not strictly along the x-direction (see Fig. S15). The results showed that only the x-component of the field contributed to enhanced salt rejection, while the y-component (perpendicular to the channel wall) had no significant effect. This is because water dipoles can easily reorient along the direction parallel to the channel wall, but are difficult to reorient in the perpendicular direction, consistent with the unusually high dielectric constant along the parallel direction and the unusually low dielectric constant along the perpendicular direction observed in recent experiments [55,56]. Moreover, we analyzed the angle between the water dipole and the direction of the applied electric field, both in the presence and absence of the field (Fig. S16). Within approximately 4 Å of the channel entrances, water dipoles show a modest but detectable alignment with the field, indicating that the applied field slightly penetrates into the adjacent bulk reservoirs. Importantly, this reorientation in the interfacial region is significantly weaker than that inside the channel and varies smoothly and continuously from the channel interior to the bulk. These observations indicate that field penetration into the reservoirs is spatially limited and physically continuous, rather than abrupt or nonphysical. In addition, we examined the effect of the electric field in the bulk solution. As shown in Fig. S17, under the same electric field, water molecules inside the confined channel exhibit stronger reorientation (corresponding to a larger effective dielectric response [56]) than those in the bulk phase. These results further confirm that the enhanced salt rejection originates from the synergistic interplay between nanoscale confinement and the applied electric field.

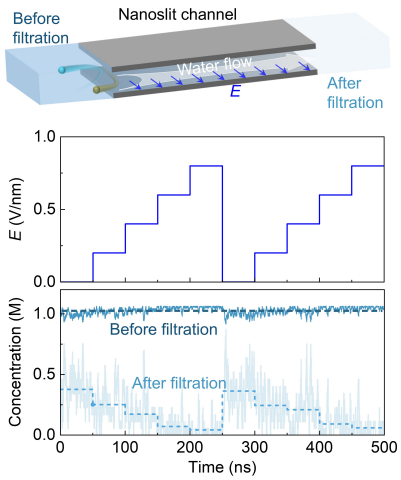


Figure 4. Schematic illustration of an electro-modulated ionic concentration regulator based on the electrically tunable selectivity. Under an electric field, the nanoslit channels exhibit tunable ion selectivity depending on the field strength (middle panel), enabling real-time control of the solution concentration after filtration without the need to alter the initial concentration (bottom panel).

In practice, a membrane containing nanoslit channels (*e.g.*, GO membranes; yellow region in Fig. 1a) can be sandwiched between two electrodes positioned on both sides of the membrane (green regions in Fig. 1a) [38,57]. The assembly can then be encapsulated with PDMS to ensure mechanical stability and prevent leakage, while keeping the inlet and outlet of the nanoslit channels open for fluid transport. After encapsulation, the device can be integrated into a microfluidic channel system and connected to an external power supply to apply a controlled electric field across the membrane [58], thereby enabling desalination. Beyond desalination, our discovery of continuously electric-field-tunable ion selectivity enables the design of electro-modulated ionic concentration regulators (Fig. 4). Additional simulations confirm that gradually varying the field strength induces synchronous shifts in permeate concentration. This ability for real-time, precise, and reversible

tuning of local ion concentrations opens up a range of unprecedented applications. For example, in lithium-ion battery manufacturing, the adjustable electrolyte concentration during the filling and formation stages is essential for tailoring the solid electrolyte interphase, enhancing the wetting of high-surface-area electrodes, and establishing beneficial concentration gradients that suppress dendrite growth [59]. Likewise, in electrochemical synthesis, dynamic concentration tuning could be used to shift reaction pathways in real-time—enhancing selectivity, suppressing parasitic reactions, and enabling stepwise synthesis of complex molecules [60].

Conclusion

In summary, we demonstrate through extensive MD simulations that an external electric field can effectively modulate the ion selectivity of nanofluidic channels. The salt rejection rate is increased from 84% to 99.5%, while maintaining the high water permeability, thereby overcoming the permeability-selectivity tradeoff. The enhanced selectivity arises from the electric field-induced reorientation of ion hydration shells within the channel, which strengthens the electrostatic repulsion between ions and the water molecules in their hydration shells, thereby increasing the energy barrier for ion permeation. This mechanism proves robust across various ion species, pressures, channel spacings, and wall materials. Beyond desalination, the proposed strategy enables active and programmable control over concentration, introducing a powerful new degree of freedom for the design of advanced electrochemical systems.

Methods

Model constructions. The graphene sheets forming the nanoslit channel shown in Fig. 1a were generated using the Nanotube Builder plugin of VMD [61]. In this work, unless otherwise specified, the nanoslit channel has a length of 6 nm. The simulation model has dimensions of 3.6 nm, 4.0 nm, and 12 nm along the x, y, and z directions, respectively, with the channel positioned at the center of the system. The solution with ions in reservoirs was built by the Solvate plugin and the Autoionize plugin of VMD [61]. The graphene oxide (GO) structures were constructed using the gmxtools [62]. The model featured 30% functionalization of carbon atoms with epoxy (-O-), hydroxyl (-OH), and carboxyl (-COOH) groups.

MD simulations. The NAMD2 software package was used to perform the MD simulations [63]. The TIP3P water model was used to describe water molecules [64]. Carbon atoms (modeled as sp2-like aromatic carbons, CA) and ions (K^+, Na^+, Ca^{2+}, Mg^{2+} and Cl^-) were described with the CHARMM36 force field [65]. Carbon atoms were set electrically neutral. The Lennard-Jones parameters of Br^- and I^- ions were taken from Ref. [66]. The CHARMM force field parameters, including atom types and partial charges, for the functionalization of GO were assigned as follows: Carboxyl (-COOH): CD ($+0.72\,e$), OB ($-0.55\,e$), OH1 ($-0.61\,e$), H ($+0.44\,e$); the bonded graphene carbon atom carries a charge of $+0.11\,e$; Hydroxyl (-OH): OH1 ($-0.54\,e$), H ($+0.43\,e$); the bonded graphene carbon atom carries a charge of $+0.11\,e$; Epoxy (-O-): O ($-0.50\,e$), each of the two neighboring graphene carbon atoms carries a charge of $+0.25\,e$. The particle mesh Ewald (PME) method was employed to compute the long-range electrostatic interactions [67]. The periodic boundary conditions were used in all directions. All carbon atoms and atoms of GO were frozen at their initial positions during the simulations. The time step was 2 fs. Each system was first energy-minimized for 5000 steps, followed by a 2 ns equilibration simulation under the NPT ensemble (1 atm, 300 K), using a Langevin piston and a Langevin thermostat to maintain pressure and temperature, respectively [68]. Subsequently, MD simulations under the NVT ensemble were performed in the presence of electric fields with magnitudes of 0, 0.05, 0.1, 0.3, 0.5, 0.8, and 1.0 V/nm. Over 200 ns of total simulation time was employed to ensure that permeability calculations converged for each simulation, with trajectories saved every 10 ps.

In classical MD simulations, the force exerted by the electric field (F_E) was directly applied to atoms according to $F_E = Eq$, where q represents the charge of the atoms. The external pressure (ΔP) was applied by exerting an external force (f) on n water molecules located in the bulk water region of $-55 < z < -45$ Å, according to the equation $\Delta P = nf/A$, where A is the area of the x-y plane [69]. In most simulations, an external pressure of 100 MPa was adopted, whereas in the simulation of the electro-modulated ionic concentration regulator the pressure was increased to 200 MPa.

US simulations. The free energy (PMF) profiles of water and ions were calculated by the US method [26]. The reaction coordinate (*i.e.*, the

movement pathway along the channel axis z) of the target water molecule or ion, spanning $-45 \leq z \leq 45$ Å, was divided into consecutive sampling windows, with a width of 1 Å. In each window, the target water molecule or ion was placed in the center and constrained by a harmonic constrain with a spring constant of 2 kcal/mol/Å^2 along the z axis. Each simulation was carried out for 3 ns, with the first 500 ps discarded before further analysis. The positional distributions in all simulations were extracted to construct the free energy profiles using the weighted histogram analysis method (WHAM) according to the implementation of Grossfield [70,71]. In the US simulations using the polarizable model, water was described by the SWM4-NDP model [72], and the Drude force field was used for describing ions and carbon atoms (modeled as type CD2R6A) [73,74]. The time step was 0.5 fs. Each simulation lasted 200 ps, with the first 50 ps discarded.

Calculation details of the Na^+-water interaction energy in ab initio MD simulations. As shown in Fig. S14, the dimensions of the simulation system in the x- and z-directions are 19.65 and 21.29 Å, respectively. In the y-direction, a vacuum layer of 30 Å was added to avoid interactions between periodic images. The system was first equilibrated using classical MD simulations for 2 ns. *Ab initio* molecular dynamics (AIMD) simulations were then performed for 1 ps without an external electric field, followed by 0.1 ps under an applied field of 1.0 V/nm. The interaction energy in each case was calculated based on the configurations of the last 10 frames (0.5 fs per frame) of AIMD simulations. Further DFT calculation on each configuration was performed to compute the total energies of the system, E_{total}, the energy of the isolated molecule (an isolated ion or water molecule), E_{isolated}, and the energy of the remaining atoms, E_{remain}. The interaction energy was then calculated as $E_{\text{int}} = E_{\text{total}} - E_{\text{isolated}} - E_{\text{remain}}$. All AIMD and DFT calculations were performed using the CP2K software package, employing the QUICKSTEP module [75,76]. The revPBE exchange–correlation functional combined with the D3(0) dispersion correction was used to account for exchange–correlation and vdW interactions [77,78]. The Goedecker–Teter–Hutter (GTH) pseudopotentials and DZVP-MOLOPT-SR-GTH basis sets were employed to describe core and valence electrons, respectively [79,80]. The time step for AIMD simulations was 0.5 fs. The *NVT* ensemble was adopted, with temperature maintained at 300 K using a Nosé–Hoover thermostat [81,82]. Periodic boundary conditions were applied in all three directions. During AIMD simulations, the carbon atoms were fixed along the y-direction. The external electric field was applied using the finite periodic electric field approach based on the Berry phase formalism. A plane-wave cutoff of 600 Ry was used in the Gaussian and plane wave (GPW) method [76]. In the AIMD and DFT calculations, the k-points were set to 1×1×1 and 2×1×2, respectively. Input files for CP2K were generated using the Multiwfn program [83].

Calculations of the salt rejection rate. The salt rejection, R‰, can be expressed as [84]:

$$\begin{aligned} R‰ &= \left(1 - \frac{C_p}{C_f}\right) \times 100‰ \\ &= \left(1 - \frac{n_{p,i}/n_{p,w}}{n_i/n_w}\right) \times 100‰, \end{aligned} \tag{1}$$

where C_p and C_f are the ion concentrations in the permeate and feed sides, $n_{p,i}$ ($n_{p,w}$) is the number of ions (water molecules) passing through the nanoslit, n_i (n_w) is the total number of ions (water molecules) in the bulk solution.

$n_{p,i}$ and $n_{p,w}$ were obtained from the converged cumulative net fluxes. The logic for calculating cumulative flux is illustrated in Fig. S18a. In each frame, the bulk solution on the feed side, the channel, and the bulk solution on the permeate side were assigned values of -1, 0, and 1, respectively. A particle that traverses the channel in the forward direction ($-1 \rightarrow 0 \rightarrow 1$) was counted as +1, whereas a particle traversing in the reverse direction ($1 \rightarrow 0 \rightarrow -1$) was counted as -1. The sum of these counts over all frames then yields the cumulative net flux through the channel. Ions that crossed the periodic boundary directly from one bulk solution to the other (i.e., $-1 \rightarrow 1$ or $1 \rightarrow -1$ without passing through 0) were excluded from the flux calculation. This procedure ensures that only true trans-channel transport contributes to the salt rejection calculation. Typical cumulative fluxes of water molecules and ions, with and without an applied electric field, are shown in Fig. S18b.

Hydration-shell structure analysis and interaction energy calculations. Hydration-shell structure analysis and interaction energy calculations were performed using the trajectories employed for the free energy calculations. In these trajectories, the ion was free to move along the x and y axes, while a harmonic constraint with a spring

constant of 2 kcal/mol/Å^2 was applied along the z axis (see details in the US simulations section), allowing us to collect sufficient data for reliable statistics.

The interaction energy calculations were performed in a manner similar to the analysis of the orientation angle distribution using the same trajectory. Specifically, the interaction energy, including both Coulomb and van der Waals contributions, between water molecules and the ion was calculated using the NAMD Energy plugin in VMD [61].

ACKNOWLEDGMENTS

This work was supported by the National Natural Science Foundation (NSF) of China (Grant Nos. 12322213, 12172170, and T2293691), the NSF of Jiangsu Province (Grant Nos. BK20230029, BK20221476, and BK20212008), the Research Fund of the State Key Laboratory of Mechanics and Control of Mechanical Structures (Grant Nos. MCAS-I-0124G01, MCAS-I-0525K01),), the Fundamental Research Funds for the Central Universities (Grant Nos. NE2022001, NC2023001, NJ2023002, and NJ2024001), and the Fund of Prospective Layout of Scientific Research for NUAA (Nanjing University of Aeronautics and Astronautics). This work was also partially supported by the High Performance Computing Platform of Nanjing University of Aeronautics and Astronautics.

DATA AVAILABILITY

The data that support the findings of this study are available from the corresponding author upon reasonable request.

COMPETING INTERESTS

There are no competing interests to declare.

REFERENCES

1. Werber JR, Osuji CO and Elimelech M. Materials for next-generation desalination and water purification membranes. *Nat. Rev. Mater.* 2016; **1**: 1–15.
2. Epsztein R, DuChanois RM, Ritt CL *et al.* Towards single-species selectivity of membranes with subnanometre pores. *Nat. Nanotechnol.* 2020; **15**: 426–436.
3. Biesheuvel P, Porada S, Elimelech M *et al.* Tutorial review of reverse osmosis and electrodialysis. *J. Membr. Sci.* 2022; **647**: 120221.
4. Ortiz-Medina J, Inukai S, Araki T *et al.* Robust water desalination membranes against degradation using high loads of carbon nanotubes. *Sci. Rep.* 2018; **8**: 2748.
5. Lee TH, Balcik M, Ali Z *et al.* Microporous polyimine membranes for efficient separation of liquid hydrocarbon mixtures. *Science* 2025; **388**: 839–844.
6. Marchetti P, Jimenez Solomon MF, Szekely G *et al.* Molecular separation with organic solvent nanofiltration: a critical review. *Chem. Rev.* 2014; **114**: 10735–10806.
7. Cohen-Tanugi D and Grossman JC. Water desalination across nanoporous graphene. *Nano Lett.* 2012; **12**: 3602–3608.
8. Wang EN and Karnik R. Graphene cleans up water. *Nat. Nanotechnol.* 2012; **7**: 552–554.
9. Koenig SP, Wang L, Pellegrino J *et al.* Selective molecular sieving through porous graphene. *Nat. Nanotechnol.* 2012; **7**: 728–732.
10. O'Hern SC, Stewart CA, Boutilier MS *et al.* Selective molecular transport through intrinsic defects in a single layer of cvd graphene. *ACS Nano* 2012; **6**: 10130–10138.
11. O'Hern SC, Boutilier MS, Idrobo JC *et al.* Selective ionic transport through tunable subnanometer pores in single-layer graphene membranes. *Nano Lett.* 2014; **14**: 1234–1241.
12. Surwade SP, Smirnov SN, Vlassiouk IV *et al.* Water desalination using nanoporous single-layer graphene. *Nat. Nanotechnol.* 2015; **10**: 459–464.
13. Jain T, Rasera BC, Guerrero RJS *et al.* Heterogeneous sub-continuum ionic transport in statistically isolated graphene nanopores. *Nat. Nanotechnol.* 2015; **10**: 1053–1057.
14. Heiranian M, Farimani AB and Aluru NR. Water desalination with a single-layer MoS_2 nanopore. *Nat. Commun.* 2015; **6**: 8616.
15. Li W, Yang Y, Weber JK *et al.* Tunable, strain-controlled nanoporous MoS_2 filter for water desalination. *ACS Nano* 2016; **10**: 1829–1835.
16. Wang Y, He Z, Gupta KM *et al.* Molecular dynamics study on water desalination through functionalized nanoporous graphene. *Carbon* 2017; **116**: 120–127.
17. Xue M, Qiu H and Guo W. Exceptionally fast water desalination at complete salt rejection by pristine graphyne monolayers. *Nanotechnology* 2013; **24**: 505720.
18. Qiu H, Xue M, Shen C *et al.* Graphynes for water desalination and gas separation. *Adv. Mater.* 2019; **31**: 1803772.
19. Hummer G, Rasaiah JC and Noworyta JP. Water conduction through the hydrophobic channel of a carbon nanotube. *Nature* 2001; **414**: 188–190.
20. Hinds BJ, Chopra N, Rantell T *et al.* Aligned multiwalled carbon nanotube membranes. *Science* 2004; **303**: 62–65.
21. Majumder M, Chopra N, Andrews R *et al.* Enhanced flow in carbon nanotubes. *Nature* 2005; **438**: 44–44.
22. Majumder M, Chopra N and Hinds BJ. Effect of tip functionalization on transport through vertically oriented carbon nanotube membranes. *J. Am. Chem. Soc.* 2005; **127**: 9062–9070.
23. Holt JK, Park HG, Wang Y *et al.* Fast mass transport through sub-2-nanometer carbon nanotubes. *Science* 2006; **312**: 1034–1037.
24. Corry B. Designing carbon nanotube membranes for efficient water desalination. *J. Phys. Chem. B* 2008; **112**: 1427–1434.
25. Fornasiero F, Park HG, Holt JK *et al.* Ion exclusion by sub-2-nm carbon nanotube pores. *Proc. Natl. Acad. Sci. U. S. A.* 2008; **105**: 17250–17255.

26. Song C and Corry B. Intrinsic ion selectivity of narrow hydrophobic pores. *J. Phys. Chem. B* 2009; **113**: 7642–7649.
27. Chan WF, Chen Hy, Surapathi A *et al.* Zwitterion functionalized carbon nanotube/polyamide nanocomposite membranes for water desalination. *Acs Nano* 2013; **7**: 5308–5319.
28. Nair R, Wu H, Jayaram PN *et al.* Unimpeded permeation of water through helium-leak–tight graphene-based membranes. *Science* 2012; **335**: 442–444.
29. Esfandiar A, Radha B, Wang F *et al.* Size effect in ion transport through angstrom-scale slits. *Science* 2017; **358**: 511–513.
30. Wang Z, Tu Q, Zheng S *et al.* Understanding the aqueous stability and filtration capability of MoS_2 membranes. *Nano Lett.* 2017; **17**: 7289–7298.
31. Gopinadhan K, Hu S, Esfandiar A *et al.* Complete steric exclusion of ions and proton transport through confined monolayer water. *Science* 2019; **363**: 145–148.
32. Kim HW, Yoon HW, Yoon SM *et al.* Selective gas transport through few-layered graphene and graphene oxide membranes. *Science* 2013; **342**: 91–95.
33. Li H, Song Z, Zhang X *et al.* Ultrathin, molecular-sieving graphene oxide membranes for selective hydrogen separation. *Science* 2013; **342**: 95–98.
34. Joshi R, Carbone P, Wang FC *et al.* Precise and ultrafast molecular sieving through graphene oxide membranes. *science* 2014; **343**: 752–754.
35. Abraham J, Vasu KS, Williams CD *et al.* Tunable sieving of ions using graphene oxide membranes. *Nat. Nanotechnol.* 2017; **12**: 546–550.
36. Celebi K, Buchheim J, Wyss RM *et al.* Ultimate permeation across atomically thin porous graphene. *Science* 2014; **344**: 289–292.
37. Wang Z, Ma C, Xu C *et al.* Graphene oxide nanofiltration membranes for desalination under realistic conditions. *Nat. Sustain.* 2021; **4**: 402–408.
38. Tiwary SK, Singh M, Chavan SV *et al.* Graphene oxide-based membranes for water desalination and purification. *npj 2D Mater. Appl.* 2024; **8**: 27.
39. Shen J, Aljarb A, Cai Y *et al.* Engineering grain boundaries in monolayer molybdenum disulfide for efficient water-ion separation. *Science* 2025; **387**: 776–782.
40. Zhang H, Liu B, Wu MS *et al.* Transport of salty water through graphene bilayer in an electric field: A molecular dynamics study. *Comput. Mater. Sci.* 2017; **131**: 100–107.
41. Razmkhah M, Moosavi F, Mosavian MTH *et al.* Does electric or magnetic field affect reverse osmosis desalination? *Desalination* 2018; **432**: 55–63.
42. Mortazavi V, Moosavi A and Nouri-Borujerdi A. Enhancing water desalination in graphene-based membranes via an oscillating electric field. *Desalination* 2020; **495**: 114672.
43. Sofos F, Karakasidis T and Sarris IE. Molecular dynamics simulations of ion drift in nanochannel water flow. *Nanomaterials* 2020; **10**: 2373.
44. Zhang Z, Li S, Mi B *et al.* Surface slip on rotating graphene membrane enables the temporal selectivity that breaks the permeability-selectivity trade-off. *Sci. adv.* 2020; **6**: eaba9471.
45. Gao H, Xu Q, Wang J *et al.* Beyond the pore size limitation of a nanoporous graphene monolayer membrane for water desalination assisted by an external electric field. *J. Phys. Chem. Lett.* 2021; **13**: 258–266.
46. Rouina M, Kariminia HR, Mousavi SA *et al.* Effect of electromagnetic field on membrane fouling in reverse osmosis process. *Desalination* 2016; **395**: 41–45.
47. Wen Q, Jia P, Cao L *et al.* Electric-field-induced ionic sieving at planar graphene oxide heterojunctions for miniaturized water desalination. *Adv. Mater.* 2020; **32**: 1903954.
48. Zhou W, Guo Y, Zhang Z *et al.* Field-induced hydration shell reorganization enables electro-osmotic flow in nanochannels. *Phys. Rev. Lett.* 2023; **130**: 084001.
49. Yang Z, Zhou Y, Feng Z *et al.* A review on reverse osmosis and nanofiltration membranes for water purification. *Polymers* 2019; **11**: 1252.
50. Yu Y, Fan J, Xia J *et al.* Dehydration impeding ionic conductance through two-dimensional angstrom-scale slits. *Nanoscale* 2019; **11**: 8449–8457.
51. Trushin M, Andreeva DV, Peeters FM *et al.* Structure and flow of low-dimensional water. *Nat. Rev. Phys.* 2025; 1–12.
52. Li H, Francisco JS and Zeng XC. Unraveling the mechanism of selective ion transport in hydrophobic subnanometer channels. *Proc. Natl. Acad. Sci. U. S. A.* 2015; **112**: 10851–10856.
53. He Z, Cui H, Hao S *et al.* Electric-field effects on ionic hydration: a molecular dynamics study. *J. Phys. Chem. B* 2018; **122**: 5991–5998.
54. Zwanzig RW. High-temperature equation of state by a perturbation method. i. nonpolar gases. *J. Chem. Phys.* 1954; **22**: 1420–1426.
55. Fumagalli L, Esfandiar A, Fabregas R *et al.* Anomalously low dielectric constant of confined water. *Science* 2018; **360**: 1339–1342.
56. Wang R, Souilamas M, Esfandiar A *et al.* In-plane dielectric constant and conductivity of confined water. *Nature* 2025; **646**: 606–610.
57. Zhou KG, Vasu K, Cherian C *et al.* Electrically controlled water permeation through graphene oxide membranes. *Nature* 2018; **559**: 236–240.
58. Chang CH and Yang RJ. Enhanced sample preconcentration in microfluidic chip using graphene oxide–nafion membrane. *Microfluid. Nanofluid.* 2016; **20**: 168.
59. Giffin GA. The role of concentration in electrolyte solutions for non-aqueous lithium-based batteries. *Nat. Commun.* 2022; **13**: 5250.
60. Liu MJ, Miller DM, Iwata UV *et al.* Tuning electrolyte composition to modulate catalytic performance in molecularly catalyzed electrochemical nitrate reduction. *ACS Electrochem.* 2025; .
61. Humphrey W, Dalke A and Schulten K. Vmd: Visual molecular dynamics. *J. Mol. Graphics* 1996; **14**: 33–38.
62. Li J. gmxtools v1 2022; .
63. Phillips JC, Braun R, Wang W *et al.* Scalable molecular dynamics with namd. *J. Comput. Chem.* 2005; **26**: 1781–1802.
64. Jorgensen WL, Chandrasekhar J, Madura JD *et al.* Comparison of simple potential functions for simulating liquid water. *J. Chem. Phys.* 1983; **79**: 926–935.
65. MacKerell Jr AD, Feig M and Brooks CL. Improved treatment of the protein backbone in empirical force fields. *J. Am. Chem. Soc.* 2004; **126**: 698–699.
66. Joung IS and Cheatham III TE. Determination of alkali and halide monovalent ion parameters for use in explicitly solvated biomolecular simulations. *J. Phys. Chem. B* 2008; **112**: 9020–9041.

67. Essmann U, Perera L, Berkowitz ML *et al.* A smooth particle mesh ewald method. *J. Chem. Phys.* 1995; **103**: 8577–8593.
68. Feller SE, Zhang Y, Pastor RW *et al.* Constant pressure molecular dynamics simulation: The langevin piston method. *J. Chem. Phys.* 1995; **103**: 4613–4621.
69. Zhu F, Tajkhorshid E and Schulten K. Pressure-induced water transport in membrane channels studied by molecular dynamics. *Biophys. J.* 2002; **83**: 154–160.
70. Kumar S, Rosenberg JM, Bouzida D *et al.* The weighted histogram analysis method for free-energy calculations on biomolecules. i. the method. *J. Comput. Chem.* 1992; **13**: 1011–1021.
71. Roux B. The calculation of the potential of mean force using computer simulations. *Comput. Phys. Commun.* 1995; **91**: 275–282.
72. Lamoureux G, Harder E, Vorobyov IV *et al.* A polarizable model of water for molecular dynamics simulations of biomolecules. *Chem. Phys. Lett.* 2006; **418**: 245–249.
73. Yu H, Whitfield TW, Harder E *et al.* Simulating monovalent and divalent ions in aqueous solution using a drude polarizable force field. *J. Chem. Theory Comput.* 2010; **6**: 774–786.
74. Lopes PE, Huang J, Shim J *et al.* Polarizable force field for peptides and proteins based on the classical drude oscillator. *J. Chem. Theory Comput.* 2013; **9**: 5430–5449.
75. VandeVondele J, Krack M, Mohamed F *et al.* Quickstep: Fast and accurate density functional calculations using a mixed gaussian and plane waves approach. *Comput. Phys. Commun.* 2005; **167**: 103–128.
76. Lippert BG, Hutter J and Parrinello M. A hybrid gaussian and plane wave density functional scheme. *Mol. Phys.* 1997; **92**: 477–488.
77. Zhang Y and Yang W. Comment on "generalized gradient approximation made simple". *Phys. Rev. Lett.* 1998; **80**: 890.
78. Smith DG, Burns LA, Patkowski K *et al.* Revised damping parameters for the d3 dispersion correction to density functional theory. *J. Phys. Chem. Lett.* 2016; **7**: 2197–2203.
79. Goedecker S, Teter M and Hutter J. Separable dual-space gaussian pseudopotentials. *Phys. Rev. B* 1996; **54**: 1703–1710.
80. VandeVondele J and Hutter J. Gaussian basis sets for accurate calculations on molecular systems in gas and condensed phases. *J. Chem. Phys.* 2007; **127**.
81. Nosé S. A unified formulation of the constant temperature molecular dynamics methods. *J. Chem. Phys.* 1984; **81**: 511–519.
82. Hoover WG. Canonical dynamics: Equilibrium phase-space distributions. *Phys. Rev. A* 1985; **31**: 1695.
83. Lu T. A comprehensive electron wavefunction analysis toolbox for chemists, multiwfn. *J. Chem. Phys.* 2024; **161**.
84. Zhang X, Wei M, Xu F *et al.* Thickness-dependent ion rejection in nanopores. *J. Membr. Sci.* 2020; **601**: 117899.

Supplementary Files

This is a list of supplementary files associated with this preprint. Click to download.

- SINSR.pdf